PHYSICAL REVIEW FLUIDS **8**, 014802 (2023)

# Modeling "crossing sea state" wave patterns in layered and stratified fluids

H. M. Yin, Q. Pan,* and K. W. Chow
*Department of Mechanical Engineering, University of Hong Kong, Pokfulam, Hong Kong*

(Received 3 May 2022; accepted 13 December 2022; published 17 January 2023)

Free surface waves with two or more spectral peaks propagating at an oblique angle to each other are commonly termed "crossing sea states". Such crossing patterns have been suggested as possible causes for rogue waves and maritime accidents. Modulation instabilities of plane waves using coupled Schrödinger or Zakharov equations have been adopted as theoretical models in the literature. Here, extensions to layered and stratified fluids are conducted. For a two-layer fluid with long-wave–short-wave resonance, crossing patterns with two short waves will enhance instability compared with the single-wave case. Analytical treatment beyond the linear instability regime is elucidated by a cascading mechanism. Growth of the higher-order harmonics eventually leads to finite-amplitude pulsating modes or breathers. Breathers subsequently exhibit a Fermi-Pasta-Ulam-Tsingou type recurrence. The time for the first formation of breathers predicted by the cascading mechanism attains excellent agreements with the full numerical simulations. A similar study is performed for a continuously stratified fluid with constant buoyancy frequency. Triad resonance with two components as a pair of oblique waves also produces enhanced instability and a preferred inclination of maximum growth rate. These crossing patterns will likely play critical roles in many wave-propagation configurations in fluid mechanics.

DOI: 10.1103/PhysRevFluids.8.014802

## I. INTRODUCTION

Oceanic waves with two or more spectral peaks propagating obliquely to each other are commonly known as "crossing sea states". Such wave systems have been suggested as possible mechanisms in the generation of large-amplitude displacements and rogue waves. There are theoretical studies, numerical simulations, and field datasets supporting this conjecture [1–9]. We shall focus on deterministic evolution systems as models in studying the dynamics of crossing sea states. The objective is to investigate such crossing wave patterns in layered and continuously stratified fluids. A brief review of existing works on "crossing patterns" for surface waves will be an instructive starting point. One route of investigation is to employ a pair of coupled nonlinear Schrödinger equations. Modulation instability growth rates are enhanced compared with the single wave-packet case. New regimes of instability as measured by the angle of inclination between the packets are possible [1,2].

Additional hydrodynamic effects can be incorporated, e.g., two carrier waves of different frequencies [3] and the influence of surface tension [4]. Stationary wave groups can be described by using just one Schrödinger equation as "hydrodynamic $X$ waves" [5]. The Zakharov equations can also be utilized as an alternative in the formulation, and the restriction to a "narrow-band" assumption can be relaxed [6]. Other perspectives include treating the nonlinear interactions of the wave components directly [7,8], and performing simulations with long-crested wave models [9]. A

---

[*] upanqing@connect.hku.hk

stochastic approach using the spectral properties of random waves has also been taken [10], but we shall stay with deterministic systems in this paper.

Crossing sea states can also be studied experimentally, and the importance of statistical parameters is pointed out [11]. One of the few scientifically recorded rogue waves, the Draupner Wave, has been reproduced in the laboratory under carefully controlled condition [12]. In terms of field data and observations, these crossing sea state scenarios have been tested in numerical "hindcast" in actual marine accidents involving ship and tanker [13,14].

The main goal here is to examine the interactions of waves propagating at an oblique direction to each other for layered and continuously stratified fluids. Critical issues include (i) if instability can be enhanced compared with a single oblique wave, and (ii) whether large transient motions (breathers and rogue waves) can be triggered. Two models will be employed. The first model is a two-layer fluid with a resonance between long and short waves. The necessary criterion is that the group velocity of the short wave matches the phase velocity of the long wave [15,16]. The case of evolution in two horizontal spatial dimensions with just one oblique short-wave envelope has been treated in the literature [17]. Experimentally, such resonance has been demonstrated in a laboratory for a layered fluid [18]. In terms of the theoretical aspects, analytical descriptions of rogue waves in both one [19,20] and two [21–26] spatial dimensions have been given.

For stratified fluids, slowly varying wave packets modeled by Schrödinger equation and triad resonance have been studied for many years [16,27,28]. The literature is truly vast. Instabilities of internal gravity wave beams and parametric subharmonic resonance have received tremendous attention [29]. We shall just mention a few recent, representative works on resonant triads. The effects of stratification profile and the rotation of the Earth can be important [30]. Inclusion of a linear shear in the background generates further intriguing dynamics [31].

The sequence of presentation can now be explained. Formulation of the long-short resonance for a two-layer fluid will be given (Sec. II). Dispersion relation and nonlinear evolution equations are derived. Modulation instability is studied. Instead of focusing on a theoretical search of solitons and rogue waves, we discuss the "cascading mechanism" [32,33]. Higher-order harmonics exponentially small initially grow at a faster rate than the fundamental mode. Eventually many modes attain roughly the same magnitude at one instant in time. A breather is formed. This analytical framework can provide a prediction on the first occurrence of breathers, an issue of significance in optics [34] as well as fluid mechanics. The breather subsequently decays. Modulation instability resumes when the amplitude is sufficiently small, triggering the onset of breathers for the second time. This repeating pattern is commonly associated with the classical problem of Fermi-Pasta-Ulam-Tsingou recurrence in physics. In the next phase, we study horizontal propagation of waves in a continuously stratified fluid with a constant buoyancy frequency (Sec. III). Triads with a crossing pattern exist between modes of different families. Modulation instability is studied. Preferential geometric configurations exist, i.e., special inclination angles with maximum growth rate can occur. Finally, conclusions are drawn (Sec. IV).

## II. LONG-WAVE–SHORT-WAVE RESONANCE IN A TWO-LAYER FLUID

### A. Formulation

A two-layer fluid is considered. We assume that a "nondimensionalization" procedure has been performed. The upper- (lower-) layer fluid has depth unity ($h$), respectively. The density of the lower (upper) fluid is taken as 1 (1–$\Lambda$), respectively ($0 < \Lambda < 1$). Gravity will be scaled to unity (Fig. 1). Cartesian "$z$" and "$x$", "$y$" axes will be the vertical and horizontal (streamwise, spanwise) directions. The linear dispersion relation for small wavy disturbances is given by [17] ($\omega =$ angular frequency, $\xi =$ wave number)

$$\begin{aligned} L(\omega, \xi) \equiv {} & \omega^4[\cosh(\xi)\cosh(\xi h) + (1-\Lambda)\sinh(\xi)\sinh(\xi h)] \\ & -\xi\omega^2[\sinh(\xi)\cosh(\xi h) + \cosh(\xi)\sinh(\xi h)] + \Lambda\xi^2\sinh(\xi)\sinh(\xi h) = 0. \end{aligned} \tag{1}$$

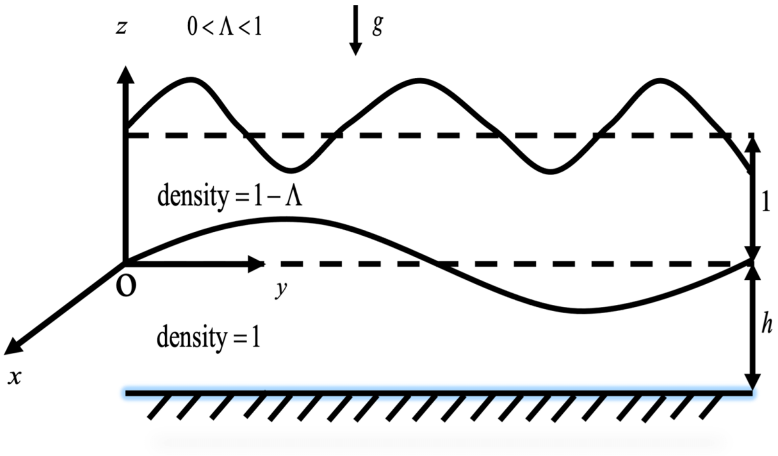

FIG. 1. Geometrical configuration of the two-layer fluid.

Two short-wave packets will propagate at an equal oblique angle ($\psi$) with respect to (but on the opposite side of) the $x$ axis. The long-wave component moves along the $x$ direction (Fig. 2). The specification of "short" and "long" refers to a ratio of the wavelength to the fluid depth. "Long-short resonance" then occurs when the projection of the group velocity of the short wave matches the phase velocity of the long wave. Asymptotic scaling requires a group velocity coordinate (Figs. 1 and 2) $x = \varepsilon^{2/3}(x^*–c_p t^*)$ and a slow time of $\tau = \varepsilon^{4/3} t^*$, with $x^*$, $y^*$, $t^*$, $\varepsilon$ being laboratory space scales, time, (small) nondimensional amplitude parameter, respectively. The relation $c_p = c_g\cos(\psi)$ holds, where "$c_p$" ("$c_g$") are the "phase (group)" velocity [15–17]. These slow spatial and temporal scales are faster than those for the nonlinear Schrödinger equation, which are $\varepsilon(x^*–c_p t^*)$ and $\varepsilon^2 t^*$. Hence, long-short resonance will be observed in a faster timeframe than the four-wave interaction scenario of the nonlinear Schrödinger equation.

The free surface displacement with two short-wave packets $S_1$, $S_2$, can be expanded asymptotically as ($S_1$, $S_2$ are functions of slow variables)

$$\varepsilon S_1 \exp\left[i(\xi_1 x^* + \xi_2 y^* - \omega t^*)\right] + \varepsilon S_2 \exp\left[i(\xi_1 x^* - \xi_2 y^* - \omega t^*)\right] + O(\varepsilon^{5/3})\ldots, \qquad \xi = \sqrt{\xi_1^2 + \xi_2^2},$$

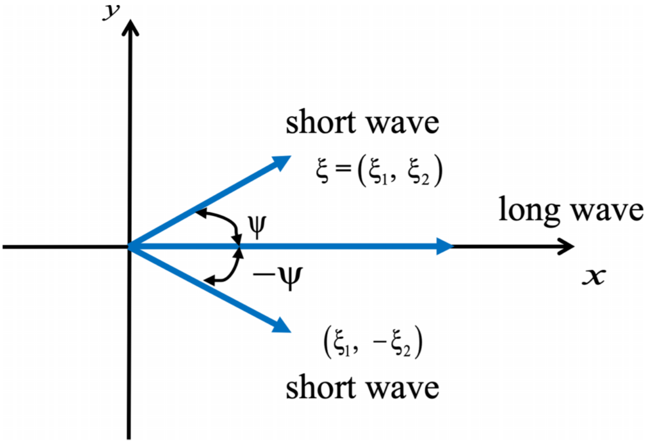

FIG. 2. Top view of the propagation directions of the long and short waves [$x$, $y$ ($z$) are the horizontal (vertical) directions].

while the long wave (or the mean flow), $L$, is on the order of $\varepsilon^{4/3}$. A derivation from first principles for the case of just one short wave in resonance with a long wave (i.e., $S_2 = 0$) had been given in the literature [17]. An examination of the perturbation calculations shows that a model for two oblique short waves in resonance with a long wave is given by

$$i\left[\frac{\partial S_1}{\partial \tau} + c_g \sin(\psi)\frac{\partial S_1}{\partial y}\right] + a\frac{\partial^2 S_1}{\partial x^2} + bLS_1 = 0, \tag{2a}$$

$$i\left[\frac{\partial S_2}{\partial \tau} - c_g \sin(\psi)\frac{\partial S_2}{\partial y}\right] + a\frac{\partial^2 S_2}{\partial x^2} + bLS_2 = 0, \tag{2b}$$

$$\frac{\partial L}{\partial \tau} = r\frac{\partial(|S_1|^2 + |S_2|^2)}{\partial x}, \tag{2c}$$

where $x(=\varepsilon^{2/3}[x^* – c_g\cos(\psi)t^*])/y(=\varepsilon^{4/3}y^*)$ are the slow spatial scales in the group velocity frame–spanwise directions, and $\tau = \varepsilon^{4/3}t$ is slow time. "$\psi$" is the angle of inclination of the short waves relative to the long wave or $x$ axis. The interaction parameters $a$, $b$, $r$ are tabulated in Appendix A.

A remark on the fluid physics of Eq. (2) is in order, especially in comparison with the classical dynamics of a weakly nonlinear, complex valued, narrow-banded wave packet ($\Phi$) governed by the nonlinear Schrödinger equation [27,35]:

$$i\partial\Phi/\partial T_2 + \partial^2\,\Phi/\partial \mathrm{w}^2 \pm |\Phi|^2\Phi = 0,\ \ T_2 = \varepsilon^2\,t^*,\ \ \mathrm{w} = \varepsilon(x^* - c_g t^*).$$

Cubic nonlinearity arises from two sources. Firstly, the fundamental frequency interacts with the second harmonic and regenerates itself at the cubic order [$O(\varepsilon^3)$]. Secondly, the mean flow ($\Phi\Phi^*$, or Stokes drift) will interact with the fundamental frequency ($\Phi$). For long-wave–short-wave resonance, the induced mean flow, $L$, is stronger asymptotically, being on the order of $O(\varepsilon^{4/3})$ instead of $O(\varepsilon^2)$. Hence, a product of the form $LS_1$ provides the only feedback to the evolution of the wave packet $S_1$ in the timescale of $\varepsilon^{4/3}t^*$. The "self-phase" and "cross-phase" modulations terms like $S_1S_1{}^*$, $S_2S_2{}^*$ become higher-order corrections. Similarly, nonlinear term like $LS_2$ will only affect the phase and development of the packet $S_2$, and will not enter in the evolution dynamics of the packet $S_1$.

Returning now to the analytical consideration of Eq. (2), the asymptotic scaling parameters in the $x$, $y$ directions are different, being $\varepsilon^{2/3}$, $\varepsilon^{4/3}$, respectively. Physically, the modulations in the spanwise ($y$) direction are longer than those in the streamwise ($x$) direction. While having the same asymptotic scaling parameters in both the $x$, $y$ directions will be more intuitively plausible, this balance is not feasible as the group velocities in the $y$ direction will be different in the present crossing sea state configuration (Fig. 2). There is then no group velocity frame where the two wave packets can "phase lock" for nonlinear effects to develop. A similar scenario also holds for optical physics, where solitons along optical fiber exhibit this "walk-off" effect if the group velocities differ drastically.

There are special parameter regimes where this asymptotic balance will fail or needs to be modified:

(i) Coefficient of the second-order dispersion in the streamwise direction becomes small or vanishes ($a \approx 0$ in Eqs. (2a), (2b)] − this case is discussed in Appendix B;

(ii) The inclination angle between the two "crossing sea pattern" wave trains becomes small [$\psi \approx 0$ in Eqs. (2a), (2b)] − this case is discussed in Appendix C.

While "long-short resonances" involving multiple short waves have been treated in the literature, existing works either ignore the second horizontal spatial dimension or focus on the solitons [19–26]. We go beyond the regime of modulation instability and the calculations of solitons in the present study. We demonstrate the existence of breathers by direct numerical simulations, and provide an analytical prediction of the first occurrence of breathers through a cascading mechanism.

### B. Modulation instability

We first study modulation instability by the standard scheme of linearized disturbance of continuous-wave solutions:

$$S_1 = \chi_1 \exp[i(q_1x + q_2y - q_3\tau)], S_2 = \chi_2 \exp[i(q_1x - q_2y - q_3\tau)], L = \chi_3, \tag{3}$$

with $q_1$, $q_2$ being the wave numbers in $x$, $y$ directions and the angular frequency being $q_3 = aq_1^2 - b\chi_3 + c_g q_2 \sin(\psi)$. The geometry dictates the relation $q_2 = q_1 \tan(\psi)$. The symbols $\chi_1$, $\chi_2$, $\chi_3$ denote the amplitudes of the short and long waves.

The modulation instability growth rate is computed by imposing disturbances:

$$\begin{aligned} S_1 = {} & \chi_1 \exp[i(q_1x + q_2y - q_3\tau)] \\ & \times\{1 + u_{11}\exp[i(\kappa_1x + \kappa_2y + \Omega\tau)] + u_{12}\exp[-i(\kappa_1x + \kappa_2y + \Omega^*\tau)]\}\text{'} \end{aligned} \tag{4a}$$

$$\begin{aligned} S_2 = {} & \chi_2 \exp[i(q_1x - q_2y - q_3\tau)] \\ & \times\{1 + u_{21}\exp[i(\kappa_1x + \kappa_2y + \Omega\tau)] + u_{22}\exp[-i(\kappa_1x + \kappa_2y + \Omega^*\tau)]\}\text{'} \end{aligned} \tag{4b}$$

$$L = \chi_3 + v_1 \exp[i(\kappa_1x + \kappa_2y + \Omega\tau)] + v_1^* \exp[-i(\kappa_1x + \kappa_2y + \Omega^*\tau)], \tag{4c}$$

where $\kappa_1$, $\kappa_2$ denote the modulation wave numbers and $\Omega$ is the modulation frequency.

Linearization of $u_{j,1},\ u_{j,2},\ v_1,\ j = 1,\ 2$ gives the matrix

$$M = \begin{pmatrix} m_{11} & 0 & 0 & 0 & b \\ 0 & m_{22} & 0 & 0 & b \\ 0 & 0 & m_{33} & 0 & b \\ 0 & 0 & 0 & m_{44} & b \\ -ir\kappa_1\chi_1^2 & -ir\kappa_1\chi_1^2 & -ir\kappa_1\chi_2^2 & -ir\kappa_1\chi_2^2 & i\Omega \end{pmatrix}, \tag{5}$$

with

$$m_{11} = -2aq_1\kappa_1 - a\kappa_1^2 - \Omega - c_g\kappa_2 \sin(\psi), m_{22} = 2aq_1\kappa_1 - a\kappa_1^2 + \Omega + c_g\kappa_2 \sin(\psi), \tag{6a}$$

$$m_{33} = -2aq_1\kappa_1 - a\kappa_1^2 - \Omega + c_g\kappa_2 \sin(\psi), m_{44} = 2aq_1\kappa_1 - a\kappa_1^2 + \Omega - c_g\kappa_2 \sin(\psi), \tag{6b}$$

and the growth rate can be obtained by insisting on nonzero disturbance amplitude.

There are four degrees of freedom for this linear stability problem, namely, carrier wave number ($q_1$), angle of inclination of the short waves to the $x$ axis ($\psi$), and the streamwise and transverse perturbation wave numbers ($\kappa_1$, $\kappa_2$).

The case of just one oblique short-wave packet, i.e., $\chi_2 = 0$, has been treated in works earlier (left plot, Fig. 3) [17]. For the present case of crossing wave patterns, we first fix the transverse perturbation wave number ($\kappa_2$). The dominant instability occurs when the short and long waves are nearly parallel ($\psi \approx 0$). However, unlike the nonlinear Schrödinger case [1], the most unstable wave numbers are shifted away from the long-wave regime (right plot, Fig. 3). Moreover, there is another unstable region around $0.7 < \psi < 0.8$ (radian), a “finger”-shaped domain which likely extends to values of high wave numbers (marked by the white dotted lines in the left plot of Fig. 3). Similar to the nonlinear Schrödinger case, we shall not elaborate further as high perturbation wave numbers will eventually make the asymptotic scaling questionable. We concentrate on the range $0 < \kappa_1 < 5$. The right plot of Fig. 3 delineates the case of two short waves and one long wave. The growth rate has increased. Crossing sea state (two oblique short waves) has thus enhanced instability, perhaps reinforcing speculation that rogue waves are more likely. Moreover, the unbounded region marked

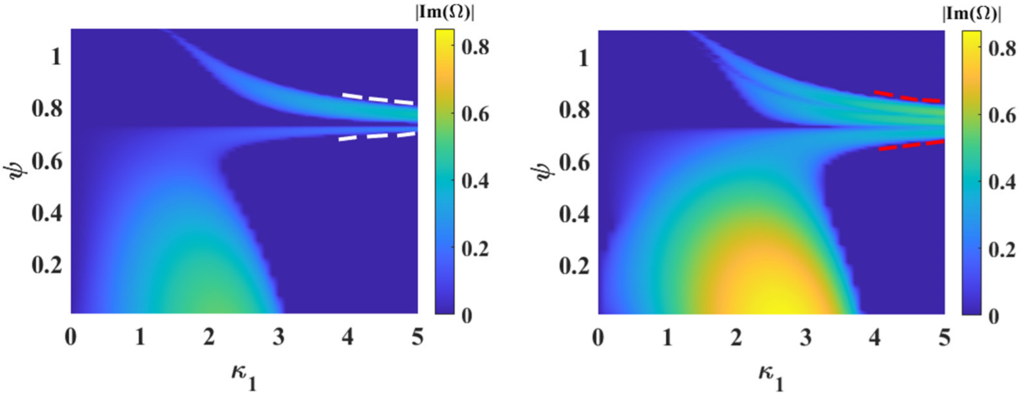

FIG. 3. Modulation instability growth rate with respect to $\kappa_1$ and $\psi$ (in radian) with parameters $q_1 = 0.2$, $\chi_1 = 1$, $\chi_2 = 0$ (left) or $\chi_2 = 1$ (right), $\Lambda = 0.5$, $h = 1$, $\kappa_2 = 2$.

with the red lines becomes broader. This implies that a larger value of $\psi$ makes the system more unstable.

We shall also examine the instability if the transverse wave number will vary too. For fixed values of $q_1 (= 0.2)$ and $\psi (= \pi/4)$, the most unstable mode actually moves further away from the long-wave regime (to $\kappa_1 \approx 5$, $\kappa_2 \approx 2$, left plot of Fig. 4). On the other hand, if we fix both $\kappa_1$ and $\kappa_2$, the modulation instability displays the largest growth rate for nearly parallel short and long waves at a modest carrier wave number ($\psi \approx 0.06$, $q_1 \approx 0.6$, right plot of Fig. 4).

As there are four possible input parameters ($q_1$, $\psi$, $\kappa_1$, $\kappa_2$), we also illustrate stability plots which show a preferential position in terms of inclination angle $\psi$. While there are ranges of parameters where the growth rates exhibit a monotonic decrease as $\psi$ increases (left plot, Fig. 5), there are ranges of the transverse wave number $\kappa_2$ for a local maximum as $\psi$ varies (middle plot, Fig. 5). Another very remarkable trend is the variation of the carrier wave number $q_1$ (right plot, Fig. 5). There can be a clear local maximum in terms of growth rate, implying a preferential crossing sea state wave number for the optimal growth of disturbances. Finally, the growth rates for two oblique waves (solid lines, Fig. 5) are bigger than those of a single oblique wave, with difference varying from, say, 10% to more than 100% (dotted lines).

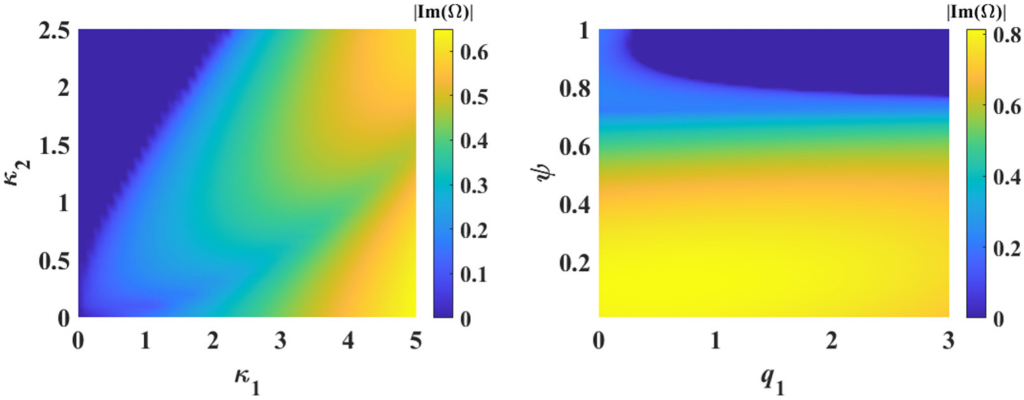

FIG. 4. Modulation instability growth rate with respect to $\kappa_1$ and $\kappa_2$, $q_1 = 0.2$, $\chi_1 = 1$, $\chi_2 = 1$, $\psi = \pi/4$, $\Lambda = 0.3$, $h = 1$ (left); Growth rate with respect to $q_1$ and $\psi$ with parameters $\chi_1 = 1$, $\chi_2 = 1$, $\Lambda = 0.3$, $h = 1$, $\kappa_1 = 2$, $\kappa_2 = 2$ (right).

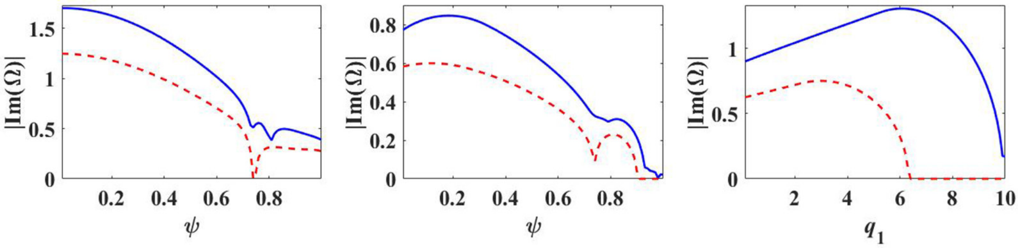

FIG. 5. Maximum modulation instability growth rate vs inclination angle $\psi$ or $x$-axis wave number $q_1$; Left: $q_1 = 2$, $\chi_1 = 1$, $\chi_2 = 1$ (solid line, blue) or $\chi_2 = 0$ (dotted line, red), $\Lambda = 0.3$, $h = 1$, $\kappa_2 = 2$, $0 \leqslant \kappa_1 \leqslant 5$; Middle: $q_1 = 2$, $\chi_1 = 1$, $\chi_2 = 1$ (solid line) or $\chi_2 = 0$ (dotted line), $\Lambda = 0.3$, $h = 1$, $\kappa_1 = 2$, $0 \leqslant \kappa_2 \leqslant 5$; Right: $\chi_1 = 1$, $\chi_2 = 1$ (solid line) or $\chi_2 = 0$ (dotted line), $\psi = \pi/4$, $\Lambda = 0.3$, $h = 1$, $\kappa_2 = 2$, $0 \leqslant \kappa_1 \leqslant 10$.

### C. Conservation laws

A few remarks on the analytical structures of the governing evolution equations [Eq. (2)] will be instructive. It is well established that conservation laws exist for nonlinear Schrödinger families of evolution equations [27,35]. Indeed, the governing equations themselves can usually be retrieved as variational derivatives of these conservation laws [36]. For the case of unidirectional propagation with only one short-wave component, i.e., $S_1 = S$, $S_2 = 0$, $\psi = 0$, i.e.,

$$iS_\tau + aS_{xx} + bLS = 0, \quad L_\tau = r(SS^*)_x,$$

there exist invariants of motion (with zero time derivative) of the form [27]

$$\int |S|^2 dx \text{ and } \int L dx.$$

The integrals can be taken over the entire domain or a finite interval, depending on whether localized or periodic boundary conditions are applied. These invariants correspond roughly to the “mass” of the system. A quadratic invariant is

$$\int \left[|S_x|^2 - bL|S|^2/a\right] dx,$$

which corresponds to the “energy” of the system.

For crossing sea states under consideration, we can derive similarly the conservation laws and the mass of the system:

$$\left(\int |S_1|^2 dx\right)_\tau + c_g \sin\psi \left(\int |S_1|^2 dx\right)_y = 0,$$
$$\left(\int |S_2|^2 dx\right)_\tau - c_g \sin\psi \left(\int |S_2|^2 dx\right)_y = 0,$$
$$\left(\int L dx\right)_\tau = 0.$$

However, we cannot find any quadratic conservation law corresponding to the energy of the unidirectional case. It is likely that the system Eq. (2) will not possess elegant structures like multisoliton and elastic collisions of localized modes.

### D. Beyond modulation instability: Formation of breathers

Modulation instability is a linear process. While growth can in principle persist indefinitely, in practice nonlinear effects will eventually need to be restored and will stop the amplification. This

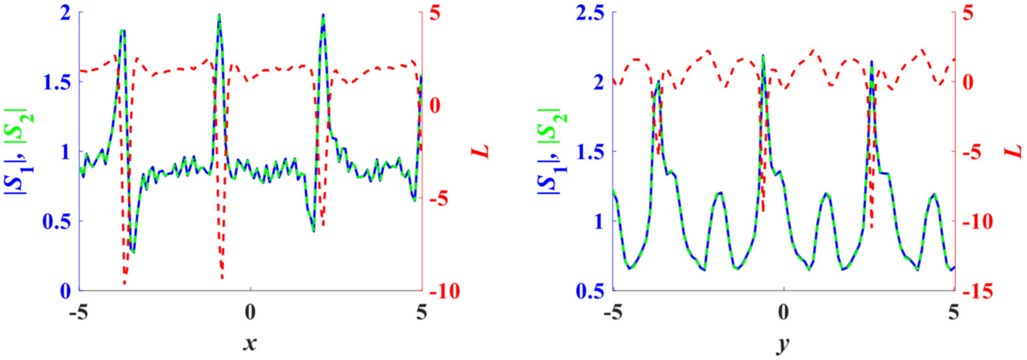

FIG. 6. Bright, bright, and dark breathers in $x$, $y$ directions (left, right plot). Parameters are $\mu = 0.01$, $q_1 = 0.2$, $\chi_1 = 1$, $\chi_2 = 1$, $\chi_3 = 1$, $\psi = 0.1$, $\Lambda = 0.3$, $h = 1$, $\kappa_1 = 2$, $\kappa_2 = 2$.

phenomenon has been studied extensively in the literature. We shall focus on just one possible route in the present dynamical evolution, namely, a cascading mechanism [32,33]. Higher-order harmonics exponentially small initially will grow at a faster rate than the fundamental one. Eventually all modes attain roughly the same order of magnitude at one instant in time. A "breather" is then observed, if we perform the numerical simulations under periodic boundary conditions. Subsequently the breather decays. On reaching sufficiently small amplitude, modulation instability is triggered again and growth resumes. The cyclic pattern is repeated and is commonly associated with the Fermi-Pasta-Ulam-Tsingou recurrence in classical physics. Dissipation or other factors may destroy this recurrence after a few cycles. This emergence of rogue waves (for unbounded domains) and breathers (under periodic boundary conditions) has been demonstrated [34,37]:

(i) numerically for many systems, e.g., nonlinear Schrödinger and Hirota equations, and
(ii) experimentally for optical fiber [34].

We shall study this phenomenon for both controlled and random initial conditions.

### 1. *Controlled initial disturbance: One single Fourier mode*

We first consider the case where the disturbance consists of one single Fourier mode. This can highlight the dynamics more effectively. In a real-world situation, the disturbance may consist of many modes or can be taken as a random noise. These situations will be studied in the future. For the single-mode case, the effect of the angle $\psi$ will be scrutinized for the emergence of breathers, under the requirement of periodic boundary conditions.

We select the initial condition as

$$S_1 = \chi_1 \exp{[i(q_1x + q_2y - q_3\tau)]} + \mu \cos{(\kappa_1 x + \kappa_2 y)}, \tag{7a}$$

$$S_2 = \chi_2 \exp{[i(q_1x - q_2y - q_3\tau)]} + \mu \cos{(\kappa_1 x + \kappa_2 y)}, \tag{7b}$$

$$L = \chi_3 + \mu \cos{(\kappa_1 x + \kappa_2 y)}, \tag{7c}$$

where $\mu$ denotes the amplitude of the perturbation. The breathers in the short-wave components display a "bright"-type pattern (peak displacement above a mean level), while the long wave shows a "dark" pattern (largest displacement below a mean level) (Fig. 6). To verify our numerical simulations, we compare the analytical and numerical spectra for the first- and second-order harmonics, i.e., the growth rate of the sideband. From Eq. (4), the amplification of the first-order harmonic of $S_1$ component is described by

$$B_1(\tau) = \mu \exp{(|\Omega_I|\tau)} = \exp{\left\{|\Omega_I|\left[\tau - \left(-\frac{\ln{(\mu)}}{|\Omega_I|}\right)\right]\right\}}, \tag{8}$$

where the growth rate $\Omega_I$ denotes the imaginary part of $\Omega$. Equation (8) can be rewritten as

$$F = \ln[B_1(\tau)] = |\Omega_I|(\tau - \tau_0),\ \tau_0 = \left(-\frac{\ln(\mu)}{|\Omega_I|}\right), \tag{9}$$

where $\tau_0$ represents an indicator for the “formation time of a breather,” i.e., time needed for $B_1$ to grow from an initial value of $\mu$ (small disturbance) to unity. With the typical parameters chosen as illustrative example, $q_1 = 0.2$, $\chi_1 = 1$, $\chi_2 = 1$, $\chi_3 = 1$, $\psi = 0.1$, $\Lambda = 0.3$, $h = 1$, $\kappa_1 = 2$, $\kappa_2 = 2$, we have $|\Omega_I| = 0.812$, $\tau_0 \approx 6$.

We shall also compute the spectra given by

$$f_{1,0}(y,\tau,\kappa_1,\kappa_2) = \frac{1}{L_1}\int_{-L_1/2}^{L_1/2} S_1(x,y,\tau)dx, \tag{10a}$$

$$f_{1,j}(y,\tau,\kappa_1,\kappa_2) = \frac{1}{L_1}\int_{-L_1/2}^{L_1/2} S_1(x,y,\tau)\exp(ij\kappa_1 x)dx,\ j = 1,2,3\ldots, \tag{10b}$$

where $f_{1,0}$ denotes the “pump” (a term borrowed from optics) of $S_1$ component, and $f_{1,\,j}$ represents the $j$th sideband.

(i) The cascading mechanism is clearly illustrated. The pump, first, second, and third harmonic all “intersect” or attain the roughly same magnitude at one particular instant in time ($\tau_0 \approx 6$). That time value also agrees with the first formation of breather from a full numerical simulation (top plot, Fig. 7).

(ii) A remark on the contrast with other classical systems is in order. For the present case, the pump reaches the minimum value at $\tau \approx \tau_0$. The sidebands also attain their peaks, but at a slightly different time instant (top plot, Fig. 7). For the extensively studied case of the nonlinear Schrödinger equation, the pump and the first sideband reach the turning points almost simultaneously at the formation time of the breather [32]. We can suggest possible explanations for this time lag. There is movement of energy among the two short waves and the long wave (middle plot, Fig. 7). There is also a transfer of energy between the $x$ and $y$ directions (bottom plot, Fig. 7).

Before we proceed to other types of wave profiles, a remark on the classification of breathers based on geometric appearance is in order. We again borrow terminology from optics. Bright (dark) pulses refer to a peak (valley) with maximum displacement above (below) the mean level. A “four-petal” mode refers to a configuration with two peaks and two valleys symmetrically placed with a saddle point in the center.

The geometric configurations of the breathers in the short-wave components also vary with the magnitude of the modulation instability. We have a sequence of pattern changes from

(i) bright (dark) breathers for $S_1$, $S_2$ ($L$) in the $x$ direction (Fig. 6) to

(ii) bright (bright) breathers for $S_1$, $S_2$ ($L$) in the $x$ ($y$) directions (Fig. 8), and finally to

(iii) four-petal (bright) breathers for $S_1$, $S_2$ ($L$) in the $x$ ($y$) directions (Figs. 9, 10).

### 2. *Symmetry breaking*

As the two short waves are placed symmetrically with respect to the long wave, identical initial conditions for the short waves will lead to the same modulus for these two wave envelopes. However, asymmetric initial conditions for the two short waves can lead to a symmetry-breaking phenomenon, i.e., different subsequent temporal evolution for $S_1$, $S_2$. As example, we choose a cosine perturbation

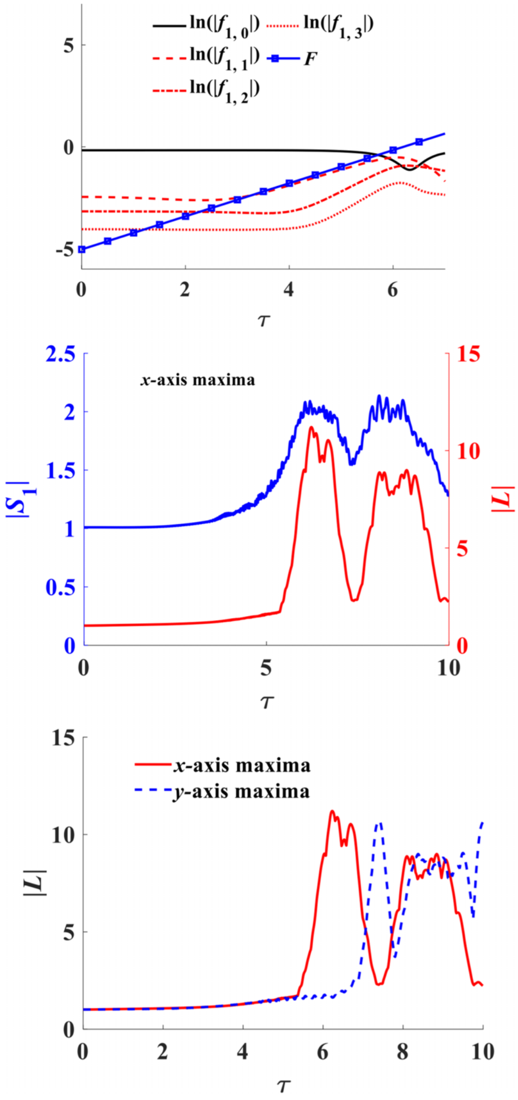

FIG. 7. Numerical and analytical spectra (top); Comparison between the $x$-axis maxima of $|S_1|$ and $|L|$ (middle); Comparison between $x$- and $y$-axis maxima of $|L|$ (bottom), with $\mu = 0.01$, $q_1 = 0.2$, $\chi_1 = 1$, $\chi_2 = 1$, $\chi_3 = 1$, $\psi = 0.1$, $\Lambda = 0.3$, $h = 1$, $\kappa_1 = 2$, $\kappa_2 = 2$.

for one and a sine function for the other:

$$S_1 = \chi_1 \exp\left[i(q_1 x + q_2 y - q_3 \tau)\right] + \mu_1 \cos\left(\kappa_1 x + \kappa_2 y\right) \tag{11a}$$

$$S_2 = \chi_2 \exp\left[i(q_1 x - q_2 y - q_3 \tau)\right] + \mu_2 \sin\left(\kappa_1 x + \kappa_2 y\right) \tag{11b}$$

$$L = \chi_3 + \mu_3 \cos\left(\kappa_1 x + \kappa_2 y\right), \tag{11c}$$

where $\mu_1$, $\mu_2$, $\mu_3$ denote the amplitude of the perturbation. This asymmetry triggers a scenario of $S_1$ (solid curve in Fig. 11) and $S_2$ (dashed curve) being distinct from each other. While the $S_1$, $S_2$ envelopes maintain the same qualitative shapes, the magnitude can differ by about 5% at the first formation time of the breather at time $\tau \approx 10.28$.

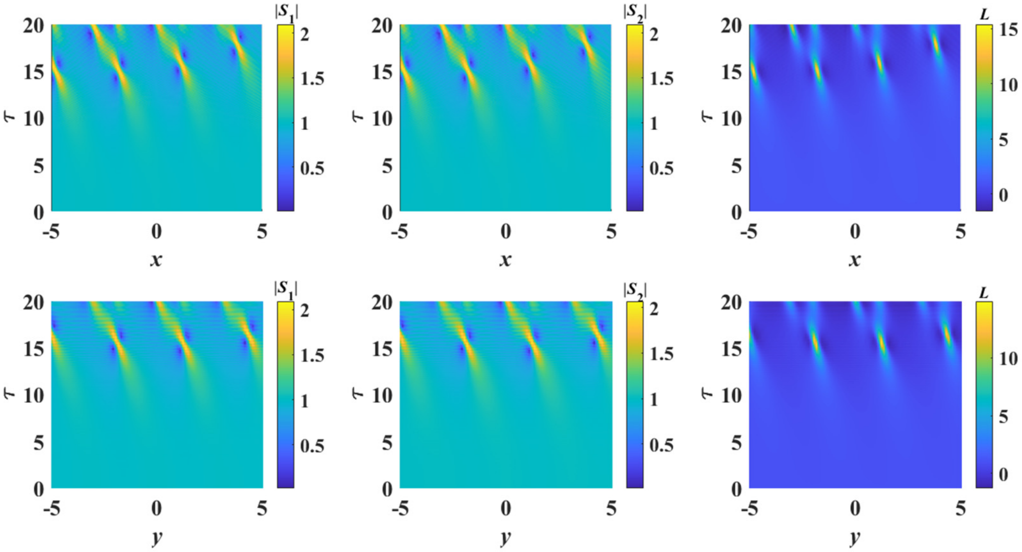

FIG. 8. Bright breather on $x$-$\tau$ (top) and $y$-$\tau$ (bottom) planes. Parameters are $\mu = 0.01$, $q_1 = 0.2$, $\chi_1 = 1$, $\chi_2 = 1$, $\chi_3 = 1$, $\psi = 0.8$, $\Lambda = 0.3$, $h = 1$, $\kappa_1 = 2$, $\kappa_2 = 2$.

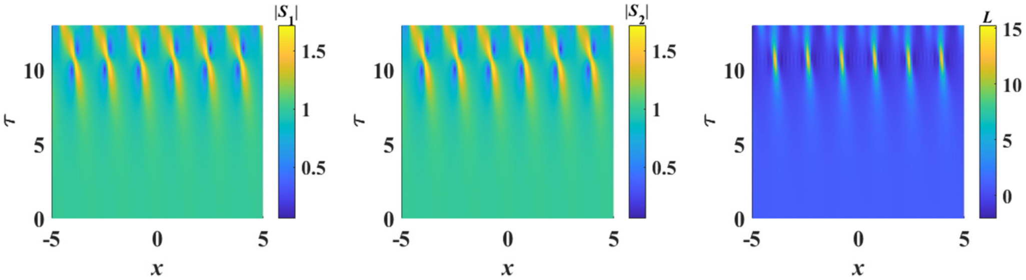

FIG. 9. Four-petal, four-petal, and bright breather on $x$-$\tau$ plane. Parameters are $\mu = 0.01$, $q_1 = 2$, $\chi_1 = 1$, $\chi_2 = 1$, $\chi_3 = 1$, $\psi = 0.78$, $\Lambda = 0.3$, $h = 1$, $\kappa_1 = 2$, $\kappa_2 = 2$.

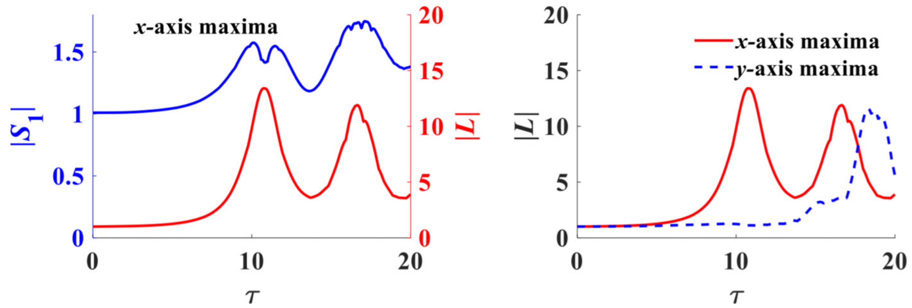

FIG. 10. Comparison between the $x$-axis maxima of $|S_1|$ and $|L|$ (left); Comparison between $x$- and $y$-axis maxima of $|L|$ (right). Parameters are $\mu = 0.01$, $q_1 = 2$, $\chi_1 = 1$, $\chi_2 = 1$, $\chi_3 = 1$, $\psi = 0.78$, $\Lambda = 0.3$, $h = 1$, $\kappa_1 = 2$, $\kappa_2 = 2$.

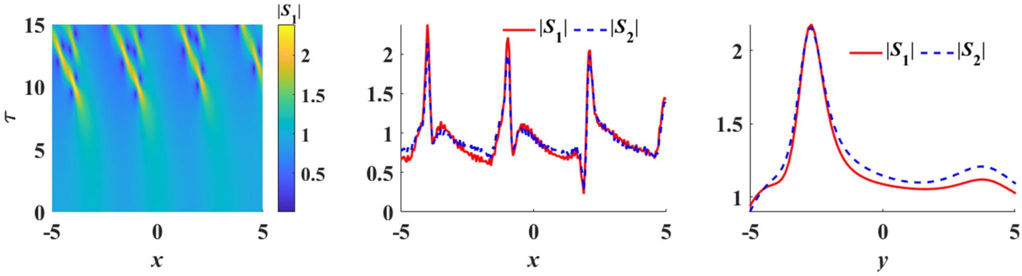

FIG. 11. Symmetry breaking: Contour plot of $|S_1|$ (left); Comparison between $|S_1|$ and $|S_2|$ in $x$ axis (middle plot) or $y$ axis (right plot) with $\tau \approx 10.28$. Parameters are $q_1 = 0.2$, $\chi_1 = 1$, $\chi_2 = 1$, $\chi_3 = 1$, $\psi = \pi/4$, $\Lambda = 0.3$, $h = 1$, $\kappa_1 = 2$, $\kappa_2 = 0.5$, $\mu_1 = 0.1$, $\mu_2 = 0.1$, $\mu_3 = 0.01$.

## III. STRATIFIED FLUIDS WITH A CONSTANT BUOYANCY FREQUENCY

### A. Formulation

Next we turn to crossing patterns which may occur for continuously stratified fluids. For simplicity, we employ a resonant triad in fluids with a constant buoyancy frequency as an illustrative example. Two components of the triad are equally inclined to the third one. The governing equations of an inviscid, incompressible, stratified fluid in usual notations are

$$\begin{aligned} u_x + v_y + w_z &= 0, \quad \rho_t + u\rho_x + v\rho_y + w\rho_z = 0, \\ \rho(u_t + uu_x + vu_y + wu_z) &= -p_x, \quad \rho(v_t + uv_x + vv_y + wv_z) = -p_y, \\ \rho(w_t + uw_x + vw_y + ww_z) &= -p_z - \rho g, \end{aligned} \tag{12}$$

with $x$, $y$ ($z$) denoting the horizontal (vertical) directions.

We first establish the linear theory for small-amplitude waves. The nonlinear dynamics of the system is then studied via the standard multiple-scale perturbation theory. The velocity component $u$ is expanded as

$$u = \varepsilon \sum_m u_1^{(m)} \exp(i\theta_m) + \varepsilon^2 \sum_m u_2^{(m)} \exp(i\theta_m), \quad \theta_m = k_m x + \beta_m y - \omega_m t, \quad m = 1, 2, 3, \tag{13}$$

where $m$ represents the three participating components of the triad, $\varepsilon$ is the small parameter defined via the ratio of wave amplitude to channel depth. The other velocity components, density and pressure, will be expanded in similar schemes. In particular, the vertical velocity is written as $w_1^{(m)} = A_m(X, Y, T)\phi_m(z)$, with $A_m(X, Y, T)$ being the slowly varying wave envelope in the slow spatial (temporal) variables $X = \varepsilon x$, $Y = \varepsilon y$, $T = \varepsilon t$, and $\phi_m(z)$ being the eigenfunction. With the Boussinesq approximation, the vertical structure of a (small-amplitude) linear wave is dictated by the eigenvalue problem for the angular frequency $\omega_m$:

$$(\phi_m)_{zz} - \left(k_m^2 + \beta_m^2\right)\phi_m + \frac{k_m^2 + \beta_m^2}{\omega_m^2} N^2 \phi_m = 0, \tag{14}$$

where $N^2 = -\frac{g}{\rho_0}\frac{d\bar{\rho}(z)}{dz}$ is the square of buoyancy frequency for the background density profile $\bar{\rho}(z)$, with the constant $\rho_0$ being the characteristic density under the Boussinesq approximation. We now assume a nondimensional coordinate system such that gravity is unity. We consider horizontal wave propagation in a rigid-wall channel of depth $H$. The boundary conditions are $\phi_m(0) = \phi_m(H) = 0$. The corresponding eigenfunction of Eq. (14) is

$$\phi_m(z) = \sin\left(\frac{n\pi z}{H}\right) \tag{15}$$

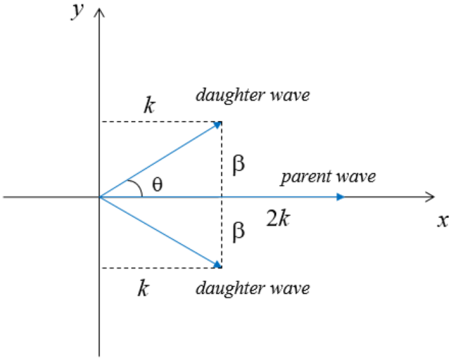

FIG. 12. Top view of three wave vectors in a stratified fluid ($z$ axis is the vertical direction).

with integer $n$ being the mode number. The dispersion relation then takes the form of

$$\omega_m^2 = \frac{(k_m^2 + \beta_m^2)N^2}{k_m^2 + \beta_m^2 + \frac{n^2\pi^2}{H^2}}. \tag{16}$$

We now search for modes which will satisfy the triad resonance condition

$$\vec{k}_1 + \vec{k}_2 = \vec{k}_3, \quad \omega_1 + \omega_2 = \omega_3. \tag{17}$$

Component 3 is termed as "parent wave," while components 1, 2 are termed as "daughter wave." The terminology in naming parent and daughter is not uniform in the literature. To achieve a crossing sea state, the wave numbers of two daughter waves are taken as oblique ones equally inclined to a mean position, i.e., $\vec{k}_1 = (k, \beta)$, $\vec{k}_2 = (k, -\beta)$. The wave number of the parent wave is $\vec{k}_3 = (2k, 0)$. The two daughter wave-number vectors are inclined at an angle of $\theta$ on either side of the the $x$ axis, with $\tan(\theta) = \frac{\beta}{k}$ (Fig. 12).

When the two daughter waves are from the same mode family $n_1$, and the parent wave is from mode family $n_3$, the triad resonance condition is written as

$$\sqrt{\frac{(k^2+\beta^2)N^2}{k^2+\beta^2+\frac{n_1^2\pi^2}{H^2}}} + \sqrt{\frac{(k^2+\beta^2)N^2}{k^2+\beta^2+\frac{n_1^2\pi^2}{H^2}}} = \sqrt{\frac{(2k)^2N^2}{(2k)^2+\frac{n_3^2\pi^2}{H^2}}}. \tag{18}$$

Straightforward calculation then gives

$$3k^4 + \left(3\beta^2 + \frac{n_3^2\pi^2}{H^2} - \frac{n_1^2\pi^2}{H^2}\right)k^2 + \frac{n_3^2\pi^2}{H^2}\beta^2 = 0, \tag{19}$$

with the solution

$$k^2 = \frac{-\left(3\beta^2 + \frac{n_3^2\pi^2}{H^2} - \frac{n_1^2\pi^2}{H^2}\right) \pm \sqrt{\left(3\beta^2 + \frac{n_3^2\pi^2}{H^2} - \frac{n_1^2\pi^2}{H^2}\right)^2 - 12\frac{n_3^2\pi^2}{H^2}\beta^2}}{6}. \tag{20}$$

To guarantee the existence of triad resonance, Eq. (20) must possess real roots. More precisely, $3\beta^2 + \frac{n_3^2\pi^2}{H^2} - \frac{n_1^2\pi^2}{H^2} < 0$ and $(3\beta^2 + \frac{n_3^2\pi^2}{H^2} - \frac{n_1^2\pi^2}{H^2})^2 - 12\frac{n_3^2\pi^2}{H^2}\beta^2 > 0$ must be satisfied. Accordingly, the constraints on $\beta$ will be

$$-\frac{\sqrt{3}\pi}{3H}(n_1 - n_3) < \beta < \frac{\sqrt{3}\pi}{3H}(n_1 - n_3), \tag{21}$$

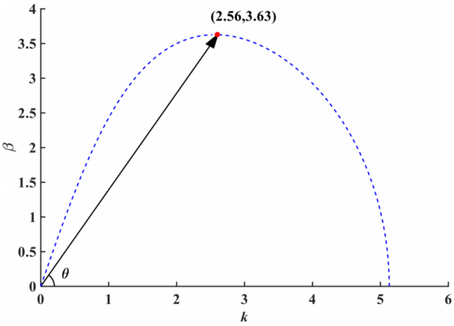

FIG. 13. All possible triads with the parameters $N^2 = 1, H = 1, n_1 = 3, n_3 = 1$.

and hence we need $n_1 > n_3$ to ensure a real $\beta$. In other words, the mode number of the daughter wave should be bigger than that of the parent wave.

The allowed combinations of $k$ and $\beta$ for buoyancy frequency $N^2 = 1$, channel depth $H = 1$, parent wave (daughter wave) mode number $n_3 = 1 (n_1 = 3)$ are illustrated (Fig. 13). The modulus of the wave vector varies with the inclination angle $\theta$ (dotted curve in Fig. 13). The maximum value of $\beta$ is 3.63, and the corresponding horizontal wave number is $k = 2.56$ with $\theta = 54.8^\circ$. There is only one set of triad for one fixed angle of inclination. This angle can range from $0^\circ$ at the right end of the curve (Fig. 13) to about $70.5^\circ$ near the origin. We should also remark on the resonance condition for the vertical wave number. The channel with rigid walls prevents vertical wave propagation and enforces standing-wave patterns as defined by Eq. (15). The choice of parent $(n_3 = 1)$ and daughter $(n_1 = 3)$ modes will not trigger any resonance in the vertical direction.

### B. Nonlinear analysis

The nonlinear development is investigated by multiple-scale perturbation method. The scheme is used widely in the literature and thus the presentation here will be brief. The first-order vertical velocity structure is given by $w_1^{(m)} = A_m(X, Y, T)\phi_m(z)$, with the corresponding expressions for the velocity components and density given as

$$u_1^{(m)} = \frac{ik_m}{k_m^2 + \beta_m^2} A_m \frac{d\phi_m}{dz}, \quad v_1^{(m)} = \frac{i\beta_m}{k_m^2 + \beta_m^2} A_m \frac{d\phi_m}{dz}, \quad \rho_1^{(m)} = -\frac{i}{\omega_m} \frac{d\bar{\rho}(z)}{dz} A_m \phi_m. \tag{22}$$

In a perturbation calculation of the equations of motion, the fluid quantities, e.g., velocities and density, are expanded in ascending powers of $\varepsilon$ (a small nondimensional parameter measuring the amplitude):

$$\begin{aligned} u = \varepsilon\big\{ & u_1^{(1)} \exp[i(kx + \beta y - \omega_1 t)] + u_1^{(2)} \exp[i(kx - \beta y - \omega_2 t)] \\ & + u_1^{(3)} \exp[i(2kx - \omega_3 t)]\big\} + \varepsilon^2 U_2 + \ldots, \end{aligned}$$

where the leading-order terms $[O(\varepsilon)]$ contain three distinct waves. The general form of the second-order term $U_2$ will contain quadratic product of the exponential phase factors $\exp[i(k_m + k_n)x + i(\beta_m + \beta_n)y – (\omega_m + \omega_n)t]$, where $k_m$, $k_n$; $\beta_m$, $\beta_n$ can be $\pm k$, $\pm\beta$, respectively. The perturbation calculations now require a linear differential operator of the higher-order terms to be solved with products of the lower-order terms as "forcing." Normally this process should be straightforward. Exceptions arise if the resonance condition [Eq. (19)] is satisfied. As example, in deriving Eq. (23a), a term $A_3 A_2{}^*$ will generate an exponential phase factor identical to that of $A_1$. This resonance condition will contribute to the dominant terms in the second order or $O(\varepsilon^2)$ calculations of the asymptotic expansion. The Fredholm alternative theorem must now be applied as the solvability conditions. Such derivations of the resonant three-wave interactions for inviscid hydrodynamic waves and even for viscous modes in a boundary layer have been documented in

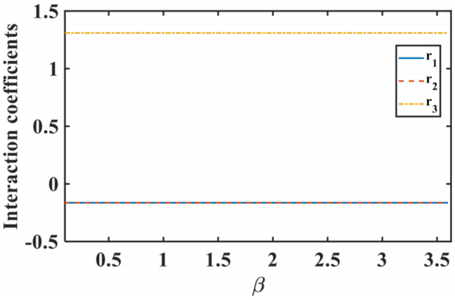

FIG. 14. Variation of the interaction coefficients with the $y$ component of wave number $\beta$, with parameters $H = 1$, $N^2 = 1$. The two daughter waves are of the same mode number $n_1 = 3$, while the parent wave is from mode $n_2 = 1$.

monographs and works in the literature [27]. The evolution equations are then derived as

$$\begin{aligned} \frac{\partial A_1}{\partial T} + V_{1x}\frac{\partial A_1}{\partial X} + V_{1y}\frac{\partial A_1}{\partial Y} &= r_1 A_3 A_2^* \\ \frac{\partial A_2}{\partial T} + V_{2x}\frac{\partial A_2}{\partial X} + V_{2y}\frac{\partial A_2}{\partial Y} &= r_2 A_3 A_1^* \\ \frac{\partial A_3}{\partial T} + V_{3x}\frac{\partial A_3}{\partial X} + V_{3y}\frac{\partial A_3}{\partial Y} &= r_3 A_1 A_2, \end{aligned} \tag{23}$$

where $V_{mx}$, $V_{my}$ are the $x$, $y$ components of the group velocity of the three members of the triad. The interaction coefficients $r_m$ are determined by lengthy formulas given in Appendix D. The interaction coefficients vary with the parameters of the fluid flow configuration, e.g., the spanwise component of the wave number $\beta$, the buoyancy frequency $N$, the channel depth $H$, as illustrated in Figs. 14–16.

The interaction coefficients can be demonstrated mathematically to be independent of the spanwise wave number $\beta$ and channel depth $H$. Take $r_3$ as an example. Employing the formulation given in Appendix D, the nonlinear terms defined through the symbols $\mathcal{H}_1^{(1,2)}$, $\mathcal{H}_2^{(1,2)}$, $\mathcal{H}_3^{(1,2)}$ can be simplified. In the numerator, the integral involving those terms will be zero from the mathematical identity ($l$, $m$, $n$ being integers):

$$\int_0^H \cos\frac{l\pi z}{H}\sin\frac{m\pi z}{H}\sin\frac{n\pi z}{H}dz.$$

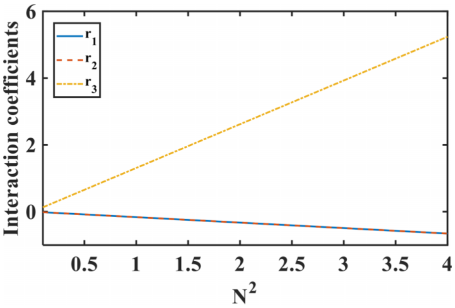

FIG. 15. Variation of the interaction coefficients with the buoyancy frequency $N$, with parameters $H = 1$, $\beta = 1$. The two daughter waves are from mode $n_1 = 3$, while the parent wave is from mode $n_3 = 1$.

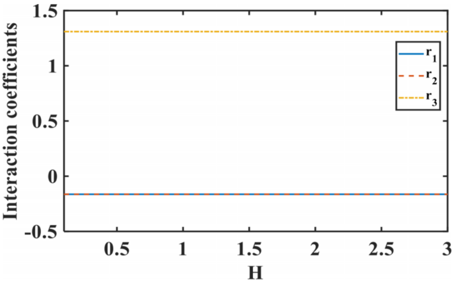

FIG. 16. Variation of the interaction coefficients with the channel depth $H$, with parameters $N^2 = 1$, $\beta = 1$. The two daughter waves are from the same mode number $n_1 = 3$, while the parent wave is from mode $n_3 = 1$.

Thus, the expression of $r_3$ can be further simplified:

$$r_3 = \frac{\int_0^H \frac{g\left(k_3^2+\beta_3^2\right)}{\bar{\rho}\omega_3} \mathcal{H}_0^{(1,2)} \phi_3 dz}{\int_0^H -\frac{2iN^2\left(k_3^2+\beta_3^2\right)}{\omega_3^2} \phi_3^2 dz} = -\frac{g\omega_3}{2iN^2} \frac{\int_0^H \frac{\mathcal{H}_0^{(1,2)}\phi_3}{\bar{\rho}} dz}{\int_0^H \phi_3^2 dz}.$$

We are working with a crossing pattern with three wave numbers of the triad as $\vec{k}_1 = (k, \beta)$, $\vec{k}_2 = (k, -\beta)$, $\vec{k}_3 = (2k, 0)$, and hence $r_3$ can be further reduced as

$$r_3 = -\frac{g\omega_3}{2iN^2} \frac{\int_0^H \frac{\mathcal{H}_0^{(1,2)}\phi_3}{\bar{\rho}} dz}{\int_0^H \phi_3^2 dz} = \frac{\omega_3 N^2}{g\omega_2} \frac{\int_0^H \sin^2\left(\frac{n_1\pi z}{H}\right) \sin\left(\frac{n_2\pi z}{H}\right) dz}{\int_0^H \sin^2\left(\frac{n_2\pi z}{H}\right) dz}.$$

Since $\frac{\omega_3}{\omega_2} = 2$ holds for all values of $\beta$, the interaction coefficients will thus be independent of the spanwise wave number when the mode number $(n_1,\ n_2)$, buoyancy frequency $(N)$, and channel depth $(H)$ are all fixed.

Evolution system Eq. (23) also permits exact solution for special circumstances, e.g., propagation in one spatial dimension only, i.e., $\partial/\partial Y \equiv 0$. Research efforts in the 1980s and 1990s had revealed exact localized solutions ("solitons") and periodic solutions in terms of the Jacobi elliptic functions [27,38]. More recent works demonstrate that Eq. (23) also possesses algebraic rogue-wave modes [39,40]. Even the lowest-order rogue wave may exhibit a quadratic or fourth-order polynomial in the denominator of the exact solutions, which will display one or two peak(s), respectively, in the wave profile.

### C. Modulation instability

The plane-wave solution of Eq. (23) is

$$\begin{aligned} A_1 &= a_1 \exp\left[i(\alpha_1 X + \gamma_1 Y - \lambda_1 T)\right], \quad A_2 = a_2 \exp\left[i(\alpha_1 X - \gamma_1 Y - \lambda_2 T)\right], \\ A_3 &= i a_3 \exp\left[i(2\alpha_1 X - (\lambda_1 + \lambda_2) T)\right]. \end{aligned} \tag{24}$$

The dispersion relation is

$$\lambda_1 = V_{1X}\alpha_1 + V_{1Y}\gamma_1 - \frac{r_1 a_3 a_2}{a_1}, \lambda_2 = V_{2X}\alpha_1 - V_{2Y}\gamma_1 - \frac{r_2 a_3 a_1}{a_2}, \lambda_1 + \lambda_2 = 2\alpha_1 V_{3X} + \frac{r_3 a_1 a_2}{a_3}. \tag{25}$$

On imposing small perturbations $a'_1, a'_2, a'_3$ in the plane-wave solution [Eq. (24)],

$$\begin{aligned} A_1 &= a_1\left(1 + a'_1\right) \exp\left[i(\alpha_1 X + \gamma_1 Y - \lambda_1 T)\right], \\ A_2 &= a_2\left(1 + a'_2\right) \exp\left[i(\alpha_1 X - \gamma_1 Y - \lambda_2 T)\right], \\ A_3 &= i a_3\left(1 + a'_3\right) \exp\left[i(2\alpha_1 X - (\lambda_1 + \lambda_2) T)\right], \end{aligned} \tag{26}$$

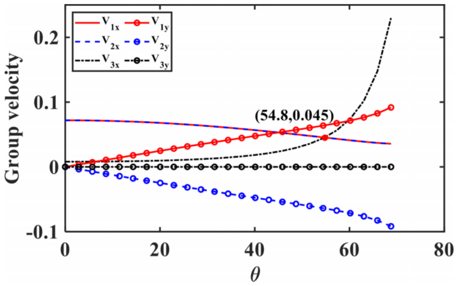

FIG. 17. Variation of group velocities of three wave components vs inclination angle $\theta$ (in °).

we formulate the small disturbances in the following form:

$$a'_m = P_m \exp\,[i(KX + BY - GT)] + iQ_m \exp\,[i(KX + BY - GT)], \quad m = 1, 2, 3, \tag{27}$$

with $K$, $B$, and $G$ being the $X$-, $Y$-wave numbers and angular frequency of the perturbations. Standard linearization will yield the requirement (superscript $T$ = transpose)

$$M_{\mathrm{triad}}[P_1 \quad P_2 \quad P_3 \quad Q_1 \quad Q_2 \quad Q_3]^T = 0. \tag{28}$$

The instability condition is a zero determinant for coefficient matrix $M_{\mathrm{triad}}$ (Appendix D).

For the parameters $n_1 = 3, n_2 = 1,\ H = 1$, and $N^2 = 1$, the interaction coefficients are given by $r_1 = r_2 = -0.1637$, $r_3 = 1.3096$. The constraint on the inclination angle $\theta$ is from 0° to 70.5°. In Eq. (23), the group velocities are defined as $V_{mx} = \frac{\partial \omega_m}{\partial k_{mx}}$, $V_{my} = \frac{\partial \omega_m}{\partial k_{my}}$. The curves of $V_{1x}, V_{2x}, V_{3x}$ intersect at $\theta = 54.8^\circ$ (Fig. 17), and the corresponding spanwise wave number of the two daughter waves reaches the maximum value (Fig. 13). For $0^\circ < \theta < 54.8^\circ$, the $x$ component of the group velocity of daughter waves is greater than that of the parent wave. Conversely, we have $V_{1x}, V_{2x} < V_{3x}$ for the range $54.8^\circ < \theta < 70.5^\circ$. Concidentally, the modulation instability reaches a minimum value at this inclination angle of $\theta = 54.8^\circ$.

Turning to the more important question of maximum growth rate, there are two input parameters, the streamwise and spanwise perturbation wave numbers [$K$ and $B$ of Eq. (27)]. We plot the angle of inclination against $K$ (Fig. 18) and $B$ (Fig. 19). In both cases, the maximum growth rate occurs in the neighborhood of $\theta = 70.5^\circ$ or the maximum angle of inclination possible.

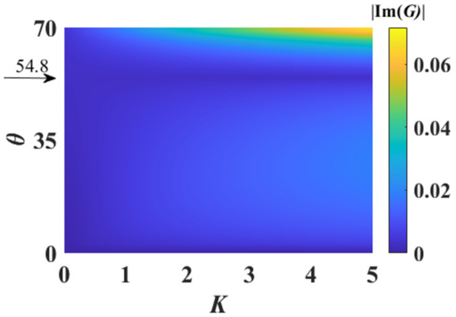

FIG. 18. Contour plot of the modulation instability growth rate: Angle of inclination $\theta$ vs the $x$-direction perturbation wave number $K$, with $a_1 = a_2 = a_3 = 1$, $r_1 = r_2 = -0.1637$, $r_3 = 1.3096$ and $y$-direction perturbation wave number $B = 1$.

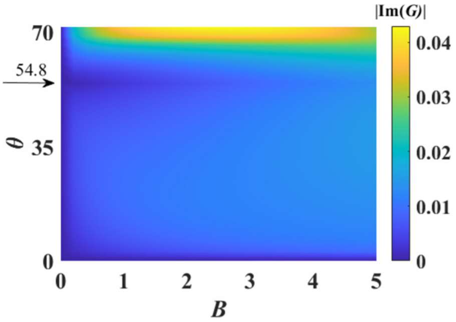

FIG. 19. Contour plot of the modulation instability growth rate: Angle of inclination $\theta$ versus the $y$-direction perturbation wave number $B$, with $a_1 = a_2 = a_3 = 1$, $r_1 = r_2 = -0.1637$, $r_3 = 1.3096$ and $x$-direction perturbation wave number $K = 2$.

Verification of these modulation instability calculations can be achieved by looking at a special case, namely, the "pump-wave" approximation regime. For simplicity, we take one-dimensional propagation, i.e., $\partial/\partial Y = 0$ in Eq. (23). If we have $|A_1|$, $|A_2| \ll 1$ and $|A_3| = O(1)$, $|A_3|$ is approximately constant ($= |A_{30}|$, say), since its derivative is quadratically small. Since $\partial^2 A_1/\partial T^2 = r_1 r_2 |A_{30}|^2 A_1$, the growth rate of a disturbance is then $(r_1 r_2)^{1/2}|A_{30}|$. Such pump-wave or "pump-beam" (a term borrowed from optics) approximation has been used extensively in the literature over the years [38,41].

In the present case, the agreement between our modulation instability calculations and values obtained from the pump-wave approximation is excellent. As an illustrative example, we choose $a_1 = a_2 = 0.1$ and $a_3 = 1$, i.e., two "small" daughter waves and a "large" parent wave. The maximum growth rate from modulation instability analysis is 0.161 (Fig. 20). If we take the pump-wave approach, the growth rate with the same parameters will give $|a_3(r_1 r_2)^{1/2}|$ or 0.1637. The error is about 1.6%. Even better accuracy is achieved for smaller $a_1$, $a_2$, say, 0.02, with errors of only 0.1%.

### D. Breathers

Similar to the two-layer situation, breathers will be formed beyond the stage of modulation instability. To highlight the emergence of these pulsating modes, a scaling transformation is first performed:

$$A_1 = \frac{\Psi_1}{\sqrt{|r_2||r_3|}}, A_2 = \frac{\Psi_2}{\sqrt{|r_1||r_3|}}, A_3 = \frac{\Psi_3}{\sqrt{|r_1||r_2|}}, T = t, x = k_x X, y = k_y Y, \tag{29}$$

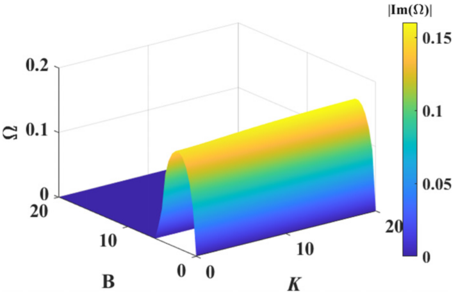

FIG. 20. Modulation instability with parameters $a_1 = a_2 = 0.1$ and $a_3 = 1$, $\theta = 70°$, $r_1 = r_2 = -0.1637$, $r_3 = 1.3096$.

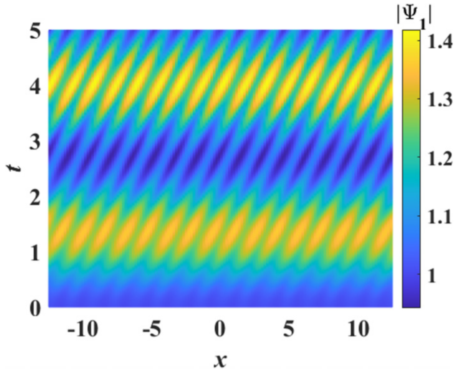

FIG. 21. Emergence of breathers for the triad resonance, with amplitude of one component $|\Psi_1|$ as example. Parameters are $a_1 = a_2 = 1$, $\alpha_1 = 2$, $\gamma_1 = 1$, $V_{1x} = 0.0709$, $V_{1y} = 0.0125$, $V_{2x} = 0.0709$, $V_{2y} = -0.0125$, $V_{3x} = 0.0084$, $V_{3y} = 0$, $k_x = 28$, $k_y = 8$, $\mu = 0.01$, $K = 2$, $B = 2$.

which will convert Eq. (23) to the normalized form ($r_1 < 0$, $r_2 < 0$, $r_3 > 0$):

$$\begin{aligned}
\frac{\partial\Psi_1}{\partial t} + k_xV_{1x}\frac{\partial\Psi_1}{\partial x} + k_yV_{1y}\frac{\partial\Psi_1}{\partial y} &= -\,\Psi_3\Psi_2^*,\\
\frac{\partial\Psi_2}{\partial t} + k_xV_{2x}\frac{\partial\Psi_2}{\partial x} + k_yV_{2y}\frac{\partial\Psi_2}{\partial y} &= -\,\Psi_3\Psi_1^*,\\
\frac{\partial\Psi_3}{\partial t} + k_xV_{3x}\frac{\partial\Psi_3}{\partial x} + k_yV_{3y}\frac{\partial\Psi_3}{\partial y} &= \Psi_1\Psi_2,
\end{aligned} \tag{30}$$

with $k_x$ and $k_y$ being arbitrary constants. Initial condition is chosen as

$$\Psi_1 = a_1 \exp\,[i(\alpha_1 x + \gamma_1 y - \lambda_1 t)] + \mu \cos\,(Kx + By), \tag{31a}$$

$$\Psi_2 = a_2 \exp\,[i(\alpha_1 x - \gamma_1 y - \lambda_2 t)] + \mu \cos\,(Kx + By), \tag{31b}$$

$$\Psi_3 = ia_3 \exp\,[i(2\alpha_1 x - (\lambda_1 + \lambda_2)t)] + \mu \cos\,(Kx + By), \tag{31c}$$

where $\mu$ is the perturbation intensity. A numerical simulation with $\theta = 10^\circ$ confirms the occurrence of breathers (Fig. 21). Symmetry breaking and cascading mechanism are expected to follow similar lines of development as outlined in previous sections.

## IV. CONCLUSIONS

Crossing sea patterns with two (or more) surface waves propagating at an oblique angle with each other have been suggested as possible causes of large displacements and marine accidents. We conjecture that such crossing patterns should also be dominant factors for other hydrodynamic wave configurations. In this work, we have tested this hypothesis for the case of layered and continuously stratified fluids under long-short and triad resonances, respectively. Instability is enhanced compared with the situation of a single wave packet. There is one (or more) preferred inclination angle(s) which permit(s) a maximum amplification rate. This property of enhanced modulation instability is commonly associated with the occurrence of rogue waves.

We go beyond the calculation of instability. We perform numerical simulations in the nonlinear regime and demonstrate the onset of breathers under periodic boundary conditions in a finite domain. Furthermore, analytical calculations leading to a cascading mechanism are demonstrated. Higher-order harmonics exponentially small initially grow faster than the fundamental mode.

Eventually all modes attain roughly the same magnitude at one instant of time. This prediction on the formation time of breathers attains excellent agreement with that from the full numerical simulations. In terms of subsequent evolution, Fermi-Pasta-Ulam-Tsingou–type recurrence is observed. The geometric configurations can change from a “bright-pulse” wave profile to a four-petal type.

We believe that similar crossing wave patterns will also enhance instability in other fluid-flow situations. One example is an improved layered-fluid model where the density is continuous and only piecewise differentiable, instead of exhibiting an abrupt jump like our present two-layer fluid [42]. This three-layer fluid will provide a better approximation for an oceanic pycnocline. Another example is the “*AB*” system arising in geophysical flows [43,44]. The mathematical structure of the *AB* equations is remarkably similar to that of the long-short case. The physics of crossing wave patterns of these situations remains to be worked out. Further exciting results are awaiting researchers.

## ACKNOWLEDGMENT

Partial financial support has been provided by the Research Grants Council General Research Fund Contracts No. HKU17200718 and No. HKU 17204722.

## APPENDIX A

The interaction coefficients in Eq. (2) for the case of one single short wave are given in earlier works [17] “$c_p$” (“$c_g$”)= “phase” (“group”) velocity of the long (short) wave. A brief outline of the derivation can be given. Typically any fluid physics entity (density, velocity, or surface displacement, denoted by $G$) can be expanded as ($\theta$ = phase of the fast oscillation)

$$G = \varepsilon G_1 e^{i\theta} + \varepsilon^{5/3} G_{2,1} e^{i\theta} + \varepsilon^{7/3} G_{3,1} e^{i\theta} + \mathrm{cc} + \varepsilon^{4/3} G_0 + \ldots\ldots \quad \text{c.c.} = \text{complex conjugate}.$$

Substitution in the equations of motion will give the linear dispersion relation and group velocity from consideration of $G_1$ and $G_{2,1}$ respectively. For calculations on $G_{3,1}$, a Fredholm alternative theorem must be applied to the inhomogeneous terms of the differential operator, leading to the evolution equation. The quantity $G_0$ represents the mean-flow effect. For the interfacial displacement, this will correspond to the long-wave component. Further details of such calculations can be found in Ref. [17] or the monographs on hydrodynamic waves [27,35].

The dynamics for the case of two short-wave packets can be worked out in a similar manner. The coefficients for the nonlinear evolution equations in the text are given by

$$\frac{\xi_1}{\xi} c_g = c_g \cos(\psi) = c_p,\; c_p^4 - (1+h)c_p^2 + \Lambda h = 0, \tag{A1}$$

$$a = \frac{1}{2}\left[\frac{dc_g}{d\xi}\cos(\psi)^2 + \frac{c_g}{\xi}\sin(\psi)^2\right], \tag{A2}$$

$$\begin{aligned} b = {} & \omega\cos(\psi)\frac{\left[\Lambda p \frac{c_g}{c_p}\left(1 - \frac{\xi^2}{\omega^4}\right)(\sigma_2 - \sigma_1) + \frac{2\Lambda\xi}{\omega c_p}\left(\frac{\xi\sigma_1}{\omega^2} - 1\right)\right]}{\left[4(1 + (1-\Lambda)\sigma_1\sigma_2) - \frac{2\xi}{\omega^2}(\sigma_1 + \sigma_2)\right]} \\ & + \omega\cos(\psi)\frac{c_p}{c_p^2 - 1}\frac{\left[-\frac{2\xi}{\omega}(1-\Lambda)(1 + \sigma_1\sigma_2) - \frac{2\Lambda\xi^2}{\omega^3}\sigma_1\left(1 - \frac{\xi}{\omega^2}\sigma_2\right)\right]}{\left[4(1 + (1-\Lambda)\sigma_1\sigma_2) - \frac{2\xi}{\omega^2}(\sigma_1 + \sigma_2)\right]} \end{aligned} \tag{A3}$$

$$\begin{aligned} r = {} & \frac{h}{2\left[(1+h)c_p^2 - 2\Lambda h\right]}\left[(1-\Lambda)c_p\left(\omega^2 - \frac{\xi^2}{\omega^2}\right) - 2(1-\Lambda)\frac{\alpha c_p^2}{\omega}\right] \\ & - \frac{h}{2\left[(1+h)c_p^2 - 2\Lambda h\right]}\left\{\frac{2\xi_1\omega}{\xi}c_p^2(1-\Lambda)\left[\cosh(\xi) - \frac{\xi}{\omega^2}\sinh(\xi)\right]\left[\sinh(\xi) - \frac{\xi}{\omega^2}\cosh(\xi)\right]\right\} \end{aligned}$$

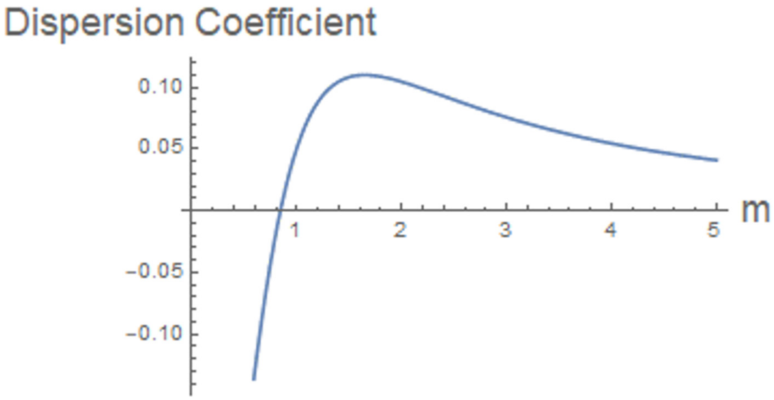

FIG. 22. Second derivative of the dispersion relation [related to the coefficient $a$ in Eqs. (2a), 2(b)] vs the spanwise wave number $m(H = 1,\ k = 1,\ \Delta = 0.1)$.

$$+\frac{h}{2\left[(1+h)c_p^2-2\Lambda h\right]}\left[\omega^2 c_p\left(1-c_p^2\right)\left(\frac{1}{\sigma_2^2}-1\right)+\frac{2\alpha\omega}{\xi\sigma_2}\left(\Lambda-c_p^2\right)\right]\left[\cosh(\xi)-\frac{\xi}{\omega^2}\sinh(\xi)\right]^2 \tag{A4}$$

$$c_g=\frac{d\omega}{d\xi},\sigma_1=\tanh(\xi),\sigma_2=\tanh(\xi h), \tag{A5}$$

where $\xi_1$ denotes wave number in $x$ direction, and $\xi$ can be evaluated with Eq. (A1).

## APPENDIX B

With the scaling of $x = \varepsilon^{2/3}[x^*–c_g\cos(\psi)t^*]$ and $y = \varepsilon^{4/3}y^*$,

(i) $\partial^2/\partial y^2[\sim O(\varepsilon^{8/3})]$ and $\partial^2/\partial x\partial y[\sim O(\varepsilon^2)]$ will normally be much smaller than $\partial^2/\partial x^2$;

(ii) values from the mixed partial derivatives $(\partial^2/\partial x\partial y)$ of functions will vanish for crossing sea state patterns: Summing mixed partial derivatives of functions using a pair of wave numbers, $\xi_+ = \xi_1\mathbf{i} + \xi_2\mathbf{j}$, $\xi_- = \xi_1\mathbf{i} - \xi_2\mathbf{j}$, $\tan\psi = \xi_2/\xi_1$, will give zero due to symmetry of the configuration.

It will be instructive to examine the value of the coefficient “$a$” in Eqs. (2a) and (2b), coefficient of the second spatial derivative in the streamwise direction (Fig. 22, plotted for typical values of depth and density ratios). In general, there is a special value of wave number where the second derivative in $x$ will vanish. Under such circumstances, an initial attempt is to adopt a different asymptotic scaling in the evolution of the short wave,

$$x=\varepsilon^{2/3}[x^*-c_g\cos(\psi)t^*],\ \ y=\varepsilon^2y^*,\ \ \tau=\varepsilon^2t^*.$$

The corresponding governing equations might be

$$i(\partial S_1/\partial\tau+c_g\sin\psi\ \partial S_1/\partial y)+a_3\partial^3S_1/\partial x^3+b_3LS_1=0,$$

$$i(\partial S_2/\partial\tau-c_g\sin\psi\ \partial S_2/\partial y)+a_3\partial^3S_2/\partial x^3+b_3LS_2=0.$$

However, such a scaling will fail as the long-wave component cannot achieve a correct balance. The precise dynamics remains to be worked out in the future. One special case which permits analytical advances is the regime of a small angle of inclination between the two crossing wave packets, to be described in Appendix C.

## APPENDIX C

If the inclination angle between the wave trains in the crossing sea pattern is small, we can achieve a different scenario of asymptotic balance. We can also drastically reduce the walk-off effect, as the difference in group velocities in the $y$ direction is then small. More precisely, if $\psi = \varepsilon^{2/3}\ \Psi_0$, where the angle $\Psi_0$ is of order 1, we can maintain the same asymptotic scaling for both $x$ and $y$. We assume (again, $*$ = order 1 laboratory coordinates)

$$x = \varepsilon^{2/3}[x^* - c_g \cos(\psi)t^*],\ Y_1 = \varepsilon^{2/3}y^*,\ \tau = \varepsilon^{4/3}t^*,$$

and the governing equations are

$$\begin{aligned}
&i(\partial S_1/\partial\tau + c_g \sin\Psi_0\ \partial S_1/\partial Y_1) + \chi_1\partial^2 S_1/\partial x^2 + \chi_2\partial^2 S_1/\partial x\partial Y_1 + \chi_3\partial^2 S_1/\partial Y_1^2 + b_3 L S_1 = 0,\\
&i(\partial S_2/\partial\tau - c_g \sin\Psi_0\ \partial S_2/\partial Y_1) + \chi_1\partial^2 S_2/\partial x^2 + \chi_2\partial^2 S_2/\partial x\partial Y_1 + \chi_3\partial^2 S_2/\partial Y_1^2 + b_3 L S_2 = 0,\\
&\partial L/\partial\tau = r_{3x}[\partial(S_1S_1^*)/\partial x + \partial(S_2S_2^*)/\partial x] + r_{3y}[\partial(S_1S_1^*)/\partial Y_1 + \partial(S_2S_2^*)/\partial Y_1].
\end{aligned}$$

For crossing sea state pattern (Fig. 2), $\chi_2$ will vanish due to symmetry and $\chi_3$ will be calculated by the second derivative of the dispersion relation with respect to the spanwise wave number:

$$\begin{aligned}
\chi_1 &= [(\partial^2\omega/\partial k^2)|_{(k,m)} + (\partial^2\omega/\partial k^2)|_{(k,-m)}]/2,\\
\chi_3 &= [(\partial^2\omega/\partial m^2)|_{(k,m)} + (\partial^2\omega/\partial m^2)|_{(k,-m)}]/2,\\
\chi_2 &= 0.
\end{aligned}$$

The new coefficients for nonlinear interaction, $r_{3x}$, $r_{3y}$, $b_3$ must be obtained from a new perturbation calculation.

Under this asymptotic regime, vanishing of the second derivative in the streamwise direction ($\chi_1 = 0$) will not present special difficulty. The second derivative in the transverse direction will provide a dispersive operator. The precise nonlinear dynamics, e.g., existence of solitons, will be examined in the future.

This analysis is based purely on asymptotic scaling. There have been many studies earlier on obliquely interacting wave trains and reflection of solitary waves from rigid walls [45]. Novel features like "Mach stem" may appear. A detailed analysis on the fluid physics when the separation angle is small should be undertaken in the future.

## APPENDIX D

The interaction coefficients of the triad equations can be calculated through a standard multiple-scale perturbation method, but the precise formulation typically involves lengthy expressions [27]. Take coefficient $r_3$ as an example:

$$\begin{aligned}
r_3 &= \frac{r_{3n}}{r_{3d}},\\
r_{3n} &= \int_0^H \left[\frac{g(k_3^2+\beta_3^2)}{\bar\rho\omega_3}\mathcal{H}_0^{(1,2)} - k_3\frac{\partial\mathcal{H}_1^{(1,2)}}{\partial z} - \beta_3\frac{\partial\mathcal{H}_2^{(1,2)}}{\partial z} + i(k_3^2+\beta_3^2)\mathcal{H}_3^{(1,2)}\right]\phi_3 dz,\\
r_{3d} &= \int_0^H -\frac{2iN^2(k_3^2+\beta_3^2)}{\omega_3^2}\phi_3^2 dz.
\end{aligned} \tag{D1}$$

The nonlinearities are

$$\begin{aligned}
\mathcal{H}_0^{(1,2)} &= u^{(1)}\big[ik_2\rho^{(2)}\big] + u^{(2)}\big[ik_1\rho^{(1)}\big] + v^{(1)}\big[i\beta_2\rho^{(2)}\big] + v^{(2)}\big[i\beta_1\rho^{(1)}\big] + w^{(1)}\rho_z^{(2)} + w^{(2)}\rho_z^{(1)},\\
\mathcal{H}_1^{(1,2)} &= u^{(1)}\big[ik_2u^{(2)}\big] + u^{(2)}\big[ik_1u^{(1)}\big] + v^{(1)}\big[i\beta_2u^{(2)}\big] + v^{(2)}\big[i\beta_1u^{(1)}\big] + w^{(1)}u_z^{(2)} + w^{(2)}u_z^{(1)},\\
\mathcal{H}_2^{(1,2)} &= u^{(1)}\big[ik_2v^{(2)}\big] + u^{(2)}\big[ik_1v^{(1)}\big] + v^{(1)}\big[i\beta_2v^{(2)}\big] + v^{(2)}\big[i\beta_1v^{(1)}\big] + w^{(1)}v_z^{(2)} + w^{(2)}v_z^{(1)},\\
\mathcal{H}_3^{(1,2)} &= u^{(1)}\big[ik_2w^{(2)}\big] + u^{(2)}\big[ik_1w^{(1)}\big] + v^{(1)}\big[i\beta_2w^{(2)}\big] + v^{(2)}\big[i\beta_1w^{(1)}\big] + w^{(1)}w_z^{(2)} + w^{(2)}w_z^{(1)}.
\end{aligned}$$

The coefficient matrix $M_{\text{triad}}$ as defined in the text [Eq. (28)] is (superscript $T$ = transpose)

$$M_{\text{triad}} = \big[M_1^T\ M_2^T\ M_3^T\ M_4^T\ M_5^T\ M_6^T\big], \tag{D2}$$

$$\begin{aligned}
M_1 &= [ia_1(-G+V_{1X}K+V_{1Y}B)\quad r_1a_2a_3\quad 0\quad -r_2a_1a_3\quad -r_3a_1a_2\quad 0],\\
M_2 &= [0\quad -r_1a_2a_3\quad ia_2(-G+V_{2X}K+V_{2Y}B)\quad r_2a_1a_3\quad -r_3a_1a_2\quad 0],\\
M_3 &= [0\quad -r_1a_2a_3\quad 0\quad -r_2a_1a_3\quad -r_3a_1a_2\quad ia_3(-G+V_{3X}K+V_{3Y}B)],\\
M_4 &= [-r_1a_2a_3\quad ia_1(-G+V_{1X}K+V_{1Y}B)\quad -r_2a_1a_3\quad 0\quad 0\quad -r_3a_1a_2],\\
M_5 &= [-r_1a_2a_3\quad 0\quad -r_2a_1a_3\quad i\rho_2(-G+V_{2X}K+V_{2Y}B)\quad 0\quad -r_3a_1a_2],\\
M_6 &= [r_1a_2a_3\quad 0\quad r_2a_1a_3\quad 0\quad i\rho_3(G-V_{3X}K-V_{3Y}B)\quad r_3a_1a_2].
\end{aligned}$$

[1] M. Onorato, A. R. Osborne, and M. Serio, Modulational Instability in Crossing Sea States: A Possible Mechanism for the Formation of Freak Waves, Phys. Rev. Lett. **96**, 014503 (2006).

[2] P. K. Shukla, I. Kourakis, B. Eliasson, M. Marklund, and L. Stenflo, Instability and Evolution of Nonlinearly Interacting Water Waves, Phys. Rev. Lett. **97**, 094501 (2006).

[3] S. Chakrabortty and S. Debsarma, Modulational instability of two obliquely interacting waves with different carrier frequencies, Phys. Fluids **33**, 127113 (2021).

[4] S. Manna and A. K. Dhar, Modulational instability of obliquely interacting capillary-gravity waves over infinite depth, Arch. Mech. **73**, 583 (2021).

[5] J. N. Steer, A. G. L. Borthwick, M. Onorato, A. Chabchoub, and T. S. van den Bremer, Hydrodynamic X Waves, Phys. Rev. Lett. **123**, 184501 (2019).

[6] O. Gramstad, E. Bitner-Gregersen, K. Trulsen, and J. C. N. Borge, Modulational instability and rogue waves in crossing sea states, J. Phys. Oceanogr. **48**, 1317 (2018).

[7] F. E. Laine-Pearson, Instability growth rates of crossing sea states, Phys. Rev. E **81**, 036316 (2010).

[8] T. A. A. Adcock, P. H. Taylor, S. Yan, Q. W. Ma, and P. A. E. M. Janssen, Did the Draupner wave occur in a crossing sea? Proc. R. Soc. A **467**, 3004 (2011).

[9] V. P. Ruban, Two different kinds of rogue waves in weakly crossing sea states, Phys. Rev. E **79**, 065304(R) (2009).

[10] S. Kundu, S. Debsarma, and K. P. Das, Wind effect on the evolution of two obliquely interacting random wave trains in deep water, Wave Motion **89**, 14 (2019).

[11] J. F. Luxmoore, S. Ilic, and N. Mori, On kurtosis and extreme waves in crossing directional seas: A laboratory experiment, J. Fluid Mech. **876**, 792 (2019).

[12] M. L. McAllister, S. Draycott, T. A. A. Adcock, P. H. Taylor, and T. S. van den Bremer, Laboratory recreation of the Draupner wave and the role of breaking in crossing seas, J. Fluid Mech. **860**, 767 (2019).

[13] L. Cavaleri, L. Bertotti, L. Torrisi, E. Bitner-Gregersen, M. Serio, and M. Onorato, Rogue waves in crossing seas: The Louis Majesty accident, J. Geophys. Res. **117**, C00J10 (2012).

[14] K. Trulsen, J. C. Nieto Borge, O. Gramstad, L. Aouf, and J.-M. Lefèvre, Crossing sea state and rogue wave probability during the Prestige accident, J. Geophys. Res. Oceans **120**, 7113 (2015).

[15] D. J. Benney, A general theory for interactions between short and long waves, Stud. Appl. Math. **56**, 81 (1977).

[16] R. Grimshaw, Modulation of an internal gravity wave packet in a stratified shear flow, Wave Motion **3**, 81 (1981).

[17] M. Oikawa, M. Okamura, and M. Funakoshi, Two-dimensional resonant interaction between long and short waves, J. Phys. Soc. Jpn. **58**, 4416 (1989).

[18] C. G. Koop and L. G. Redekopp, The interaction of long and short internal gravity waves: Theory and experiment, J. Fluid Mech. **111**, 367 (1981).

[19] K. W. Chow, H. N. Chan, D. J. Kedziora, and R. H. J. Grimshaw, Rogue wave modes for the long wave–short wave resonance model, J. Phys. Soc. Jpn. **82**, 074001 (2013).

[20] S. Chen, P. Grelu, and J. M. Soto-Crespo, Dark- and bright-rogue-wave solutions for media with long-wave–short-wave resonance, Phys. Rev. E **89**, 011201(R) (2014).

[21] S. Chen, J. M. Soto-Crespo, and P. Grelu, Coexisting rogue waves within the $(2+1)-$component long-wave–short-wave resonance, Phys. Rev. E **90**, 033203 (2014).

[22] K. Sakkaravarthi, T. Kanna, M. Vijayajayanthi, and M. Lakshmanan, Multicomponent long-wave–short-wave resonance interaction system: Bright solitons, energy-sharing collisions, and resonant solitons, Phys. Rev. E **90**, 052912 (2014).

[23] J. Chen, Y. Chen, B.-F. Feng, and K. Maruno, Multi-dark soliton solutions of the two-dimensional multi-component Yajima–Oikawa systems, J. Phys. Soc. Jpn. **84**, 034002 (2015).

[24] J. Chen, Y. Chen, B.-F. Feng, and K. Maruno, Rational solutions to two- and one-dimensional multicomponent Yajima-Oikawa systems, Phys. Lett. A **379**, 1510 (2015).

[25] H. N. Chan, E. Ding, D. J. Kedziora, R. Grimshaw, and K. W. Chow, Rogue waves for a long wave-short wave resonance model with multiple short waves, Nonlinear Dyn. **85**, 2827 (2016).

[26] J. Rao, T. Kanna, and J. He, A study on resonant collision in the two-dimensional multi-component long-wave–short-wave resonance system, Proc. R. Soc. A **478**, 2258 (2022).

[27] A. D. D. Craik, *Wave Interactions and Fluid Flows* (Cambridge University Press, Cambridge, 1985).

[28] A. K. Liu and D. J. Benney, The evolution of nonlinear wave trains in stratified shear flows, Stud. Appl. Math. **64**, 247 (1981).

[29] T. Dauxois, S. Joubaud, P. Odier, and A. Venaille, Instabilities of internal gravity wave beams, Annu. Rev. Fluid Mech. **50**, 131 (2018).

[30] B. R. Sutherland and R. Jefferson, Triad resonant instability of horizontally periodic internal modes, Phys. Rev. Fluids **5**, 034801 (2020).

[31] L. Biswas and P. Shukla, Resonant triad interactions in a stably stratified uniform shear flow, Phys. Rev. Fluids **7**, 023904 (2022).

[32] S. A. Chin, O. A. Ashour, and M. R. Belić, Anatomy of the Akhmediev breather: Cascading instability, first formation time, and Fermi-Pasta-Ulam recurrence, Phys. Rev. E **92**, 063202 (2015).

[33] H. M. Yin, Q. Pan, and K. W. Chow, Four-wave mixing and coherently coupled Schrödinger equations: Cascading processes and Fermi–Pasta–Ulam–Tsingou recurrence, Chaos **31**, 083117 (2021).

[34] G. Van Simaeys, P. Emplit, and M. Haelterman, Experimental study of the reversible behavior of modulational instability in optical fibers, J. Opt. Soc. Am. B **19**, 477 (2002).

[35] C. C. Mei, *The Applied Dynamics of Ocean Surface Waves* (World Scientific, Singapore, 1983).

[36] Z. Mu, Haochen Li, and Y. Wang, A novel energy-preserving scheme for the coupled nonlinear Schrödinger equations, Int. J. Comput. Math. **95**, 61 (2018).

[37] H. N. Chan and K. W. Chow, Rogue waves for an alternative system of coupled Hirota equations: Structural robustness and modulation instabilities, Stud. Appl. Math. **139**, 78 (2017).

[38] D. J. Kaup, A. Reiman, and A. Bers, Space-time evolution of nonlinear three-wave interactions. I. Interaction in a homogeneous medium, Rev. Mod. Phys. **51**, 275 (1979).

[39] F. Baronio, M. Conforti, A. Degasperis, and S. Lombardo, Rogue Waves Emerging from the Resonant Interaction of Three Waves, Phys. Rev. Lett. **111**, 114101 (2013).

[40] S. Chen, F. Baronio, J. M. Soto-Crespo, P. Grelu, and D. Mihalache, Versatile rogue waves in scalar, vector, and multidimensional nonlinear systems, J. Phys. A: Math. Theor. **50**, 463001 (2017).

[41] D. O. Mora, E. Monsalve, M. Brunet, T. Dauxois, and P.-P. Cortet, Three-dimensionality of the triadic resonance instability of a plane inertial wave, Phys. Rev. Fluids **6**, 074801 (2021).

[42] A. Purkait and S. Debsarma, Modulational instability of two obliquely interacting waves in presence of a thin pycnocline, Eur. J. Mech. B Fluids **84**, 517 (2020).

[43] Z. W. Xu, G.-F. Yu, and Z. N. Zhu, Bright-dark soliton solutions of the multi-component AB system, Wave Motion **83**, 134 (2018).

[44] X. G. Geng, J. Shen, and B. Xue, Dynamical behaviour of rogue wave solutions in a multi-component AB system, Wave Motion **89**, 1 (2019).

[45] K. Nakayama, T. Kakinuma, and H. Tsuji, Oblique reflection of large internal solitary waves in a two-layer fluid, Eur. J. Mech. B Fluids **74**, 81 (2019).